44th AIAA Aerospace Sciences Meeting and Exhibit
9 - 12 January 2006, Reno, Nevada

AIAA 2006-1107

Numerical Simulation and Experiment Comparison of Leading-Edge Receptivity of A Mach 5.92 Boundary Layer

Xiaowen Wang * **and Xiaolin Zhong** †
Mechanical and Aerospace Engineering Department
University of California, Los Angeles, California 90095

Abstract

In this paper, both the steady base flow and unsteady forcing flows of a Mach 5.92 boundary layer on a flat plate, corresponding to Maslov et al.'s[1] leading-edge receptivity experiments, is studied. The objective of this study is to numerically investigate the steady base flow and the receptivity of the hypersonic boundary layer, and to evaluate the accuracy of the numerical simulation by comparing the results of numerical simulations and experiments. The steady base flow is simulated by solving the two-dimensional Navier-Stokes equations with a combination of a fifth-order shock-fitting method and a second-order TVD method. The numerical solution to the steady base flow is compared with that of the experiment. The good agreement between the two sets of steady base flows indicates that the numerical simulation of the fifth-order shock-fitting method is accurate for the hypersonic flow simulation. According to the properties of the electric pulse generator used in Maslov et al.'s experiments, a model of forcing disturbances is proposed. For unsteady simulations, disturbances of six different cases are introduced to the steady base flow by a forcing slot located on the flat plate. The subsequent responses of the hypersonic boundary layer are simulated by the fifth-order shock-fitting method. The numerical results show that the hypersonic boundary-layer flow is much more sensitive to blowing-suction disturbances than to wall oscillations and energy perturbations. The pressure perturbations of wall blowing-suction is higher than that of wall oscillation. In turn, the pressure perturbations of wall oscillation is higher than that of energy perturbations. The amplitude of the pressure perturbation to energy disturbances is proportional to the energy introduced to the steady base flow.

Introduction

The performance and control of supersonic and hypersonic vehicles are significantly affected by the laminar-turbulent transition of the boundary-layer flows over the vehicle surfaces, due to the fact that a turbulent flow generates much higher shear force and heat flux on the wall than a laminar flow. Therefore, the accurate prediction of the transition location is of critical importance for the drag evaluation and aerothermal design of high-speed vehicles.

During the past decades, boundary-layer transitions have been extensively studied, and different methods are proposed to predict the transition location. Progress made in transition prediction methodology was recently reviewed by Malik[2]. In extremely low-disturbance environments, the most widely used transition prediction method is the e^N method, which is a semi-empirical method based on the linear stability theory (LST). In e^N method, the boundary-layer transition is assumed to occur when the total amplification of the most unstable normal mode exceeds some empirical factor e^N. The total amplification is defined as the ratio of amplitudes at the transition point and the lower neutral point. For supersonic and hypersonic boundary layers, the most unstable mode is generally mode S. The e^N transition prediction method works well for flows in a relatively quiet environment, where the transition is caused by the linear growth of the most unstable mode instead of by-pass transition. The success of the e^N method depends on the condition that the growth rates of the most unstable mode can be accurately predicted by LST. The correlation of series of experimental measurements of transition locations over plates, wings, and wedges shows that the typical value of N is between 8 and 11. Despite its widely application, the e^N method has a drawback, because only the linear growth of the most unstable mode is taken into account. The effects of the experimental environment and model geometry on the excitation of the unstable modes are not considered.

In an environment of small initial disturbances, the transition of the boundary-layer flow over a smooth surface from laminar to turbulent generally consists of the following three stages:

- Stage 1: Receptivity process during which small environmental disturbances enter the boundary layer and excite unstable modes;
- Stage 2: Linear development or growth of

*Graduate Student Researcher,Mechanical and Aerospace Engineering Department, Member AIAA

†Professor, Mechanical and Aerospace Engineering Department,Associate Fellow AIAA.

boundary-layer unstable modes which can be obtained by solving the eigen-problem of the homogeneous linearized stability equations;

- Stage 3: Boundary-layer transition from laminar to turbulent caused by three-dimensional and nonlinear effects occurring in the form of secondary instabilities when the unstable modes reach certain amplitudes.

According to the three-stage transition mechanism, the study of receptivity process is important, because it provides initial conditions of amplitude, frequency, and phase angle for boundary-layer normal modes[3]. The receptivity process of supersonic and hypersonic boundary-layer flows is more complex than that of subsonic boundary-layer flows due to the effects of shock wave, non-parallel flow, and high temperature, etc. In 1975, Mack[4] used the compressible linear stability theory to calculate the amplitude ratio of constant-frequency disturbances for insulated and cooled-wall flat plate boundary layers between Mach number 1.3 and 5.8. The amplitude ratio as a function of Reynolds number was used to examine the consequence of using a fixed disturbance amplitude of the most unstable frequency as a transition criterion. It was found that the transition Reynolds number with cooling obtained in his calculation increases much faster than that observed experimentally. The results proved that the stability theory alone is inadequate to determine what will happen to the particular disturbances in a given flow situation, and it is necessary to consider the properties of the external disturbances responsible for the transition. Fedorov and Khokhlov[5] studied the leading-edge receptivity of supersonic boundary-layer flows to free-stream acoustic waves by an asymptotic method. It was shown that the acoustic waves synchronize with the normal modes of supersonic boundary layers and induce the normal modes near the leading edge. In their later study[6], two receptivity mechanisms to acoustic waves at the leading edge, diffraction and diffusion, are proposed.

Demetriades[7] carried out an experimental study of the stability of a laminar hypersonic boundary layer in later 1950s. The stream-wise variations of natural and artificial disturbances were measured by a hot-wire anemometer. The artificial disturbances were generated by mechanical devices of the siren type. It was found for both natural and artificial disturbances that the small fluctuations increase for certain ranges of Reynolds number and frequency. Laufer and Vrebalovich[8] investigated the self-excited oscillations in a supersonic laminar boundary layer over an insulated flat plate. It was shown empirically that the stability limits expressed in terms of the boundary-layer-thickness Reynolds number are independent of the Mach number. It only depends on oscillation frequencies. The results also showed that the compressible boundary layer is more stable than the incompressible one. Kendall[9] experimentally studied the origin and growth of natural fluctuations in zero pressure-gradient boundary layers of several Mach numbers between 1.6 and 8.5. Substantial flow fluctuations were observed within the laminar boundary layer upstream of locations where instability amplification was expected to be important. These fluctuations were found to be correlated with the sound field for higher supersonic speeds. The growth rates of these fluctuations in the Reynolds number range upstream of the non-linearity region are in a reasonable agreement with the stability theories of Mack. In these experiments, the disturbances were not well controled. Therefore, the results could hardly be uniquely interpreted, and they could hardly be compared with theoretical results. Kosinov and Maslov[10] induced artificial disturbances of adjustable amplitude by an electric discharge in a supersonic boundary layer. The Fourier components of the wave packet were determined. The experimental data were compared with the results of LST in a parallel flow approximation. It was found that the artificial disturbances result in intensity increase of the boundary-layer pulsations. Maslov and Seminov[11] studied the receptivity of a supersonic boundary layer to artificial acoustic waves by utilizing two parallel flat plates as shown in Fig. 1. The acoustic waves generated by an electric discharge system on the lower plate radiated into the external flow and penetrated into the boundary layer of the upper plate as free-stream acoustic disturbances. It was found that the external acoustic waves are converted into boundary-layer oscillations most efficiently at the leading edge, in the neighborhood of the acoustic branch of the neutral curve, and in the vicinity of the lower branch of the neutral curve. Recently, a similar experiment was carried out for a Mach 5.92 flow by Maslov et al.[1] to study the leading-edge receptivity of the hypersonic boundary layer. It was found that Tollmien-Schlichting waves are generated by the acoustic waves impinging on the leading edge. They also found that the receptivity coefficients depend on the wave inclination angles.

With the development of advanced computers and numerical techniques, numerical simulation of the receptivity process by directly solving full Navier-Stokes equations has become feasible. Zhong[12] studied the acoustic receptivity of a hypersonic flow over a parabola by solving full Navier-Stokes equations. It was concluded that the generations of boundary-layer normal modes are mainly due to the interaction of the boundary layer with the transmitted acoustic waves instead of entropy and vorticity waves. In a series of papers, Ma and Zhong[13, 14, 15] studied the receptivity mechanisms of a supersonic boundary layer to free-stream disturbances by a combination of numerical simulation and linear stability theory. It was found that, in addition to the conventional first and second Mack modes, there exist a family of stable modes in the supersonic boundary

layer which play an important role in the excitation of unstable Mack modes. Egorov et al.[16] developed a numerical algorithm and applied it to the numerical simulation of unsteady two-dimensional flow fields relevant to transition at supersonic and hypersonic speeds. For small forcing amplitudes, the second-mode growth rates predicted by numerical simulation agree well with those resulted from LST including non-parallel effects. The results of their numerical simulation predict a non-linear saturation of fundamental harmonic and rapid growth of higher harmonics. Wang and Zhong[17, 18] studied the receptivity of a Mach 8 flow over a sharp wedge with a half angle of 5.3° to wall blowing-suction by numerical simulation and by LST. The effects of frequency and location of the blowing-suction actuator on the receptivity process are investigated by considering seven cases of different blowing-suction locations with 15 frequencies for each case. The numerical results show that mode S is the dominant boundary-layer normal mode excited by wall blowing-suction disturbances. The frequency of the blowing-suction actuator has a significant effect on the receptivity process mainly due to the frequency dependence of the synchronization point of mode F and mode S. The numerical results also show that mode S is strongly excited only when the blowing-suction actuator is located upstream of the synchronization point. When the blowing-suction actuator is downstream of the synchronization point, there is very little excitation of mode S, despite the fact that the blowing-suction actuator is still located within the unstable region of mode S. Theoretical analysis and comparisons with numerical simulations are reported by Tumin, Wang, and Zhong[19, 20]. The perturbation flow field downstream of the blowing-suction actuator is decomposed into normal modes with the help of the biorthogonal eigenfunction system. Filtered-out amplitudes of two discrete normal modes of interest agree well with the linear receptivity problem solution.

The objective of this study is to numerically investigate the steady base flow and the receptivity of the hypersonic boundary layer, and to evaluate the accuracy of the numerical simulation by comparing the results of numerical simulations and experiments. Such kind of comparison and evaluation is of great importance because numerical simulation has become a most powerful approach in stability and transition studies of supersonic and hypersonic boundary-layer flows. The steady base flow is simulated by solving the two-dimensional Navier-Stokes equations with a combination of a fifth-order shock-fitting method and a second-order TVD method. According to the properties of the electric pulse generator used in Maslov et al.'s experiments, a model of forcing disturbances is proposed. For unsteady simulations, disturbances of six different cases are introduced to the steady base flow by a forcing slot located on the flat plate, corresponding to the location of the electric pulse generator in experiments. The subsequent responses of the hypersonic boundary layer are simulated by the fifth-order shock-fitting method.

Governing equations and numerical methods

In the current numerical simulations, a Mach 5.92 flow over two parallel flat plates as shown in Fig. 2 is considered. The Mach 5.92 flow is assumed to be thermally and calorically perfect. The governing equations for the simulation are the two-dimensional Navier-Stokes equations in the conservative form, i.e.,

$$\frac{\partial \vec{U}^*}{\partial t^*} + \frac{\partial}{\partial x_1^*}(\vec{F}_{1i}^* + \vec{F}_{1v}^*) + \frac{\partial}{\partial x_2^*}(\vec{F}_{2i}^* + \vec{F}_{2v}^*) = 0 \qquad (1)$$

where the superscript "$*$" represents the dimensional variables. $\vec{U}^*$ is a vector containing the conservative variables of mass, momentum and energy. $\vec{F}_{1i}^*$ and $\vec{F}_{2i}^*$ are inviscid flux vectors, while $\vec{F}_{1v}^*$ and $\vec{F}_{2v}^*$ are viscous flux vectors. Flux vectors can be expressed as

$$\vec{F}_{ji}^* = \begin{bmatrix} \rho^* u_j^* \\ \rho^* u_1^* u_j^* + p^* \delta_{1j} \\ \rho^* u_2^* u_j^* + p^* \delta_{2j} \\ u_j^*(e^* + p^*) \end{bmatrix} \qquad (2)$$

$$\vec{F}_{jv}^* = \begin{bmatrix} 0 \\ -\tau_{1j}^* \\ -\tau_{2j}^* \\ -\tau_{nj}^* u_n^* - k^* \frac{\partial T^*}{\partial x_j^*} \end{bmatrix} \qquad (3)$$

with $j, n \in \{1, 2\}$. With the perfect gas assumption, pressure and energy are given by

$$p^* = \rho^* R^* T^* \qquad (4)$$

$$e^* = \rho^* c_v^* T^* + \frac{\rho^*}{2}(u_1^{*2} + u_2^{*2}) \qquad (5)$$

where c_v^* is the specific heat at constant volume. For compressible Newtonian flow, the viscous stress tensor can be writen as:

$$\tau_{ij}^* = \mu^*(\frac{\partial u_i^*}{\partial x_j^*} + \frac{\partial u_j^*}{\partial x_i^*}) - \frac{2}{3}\mu^* \frac{\partial u_n^*}{\partial x_n^*}\delta_{ij} \qquad (6)$$

for $i, j, n \in \{1, 2\}$. In the simulation, the viscosity coefficient, μ^*, and the heat conductivity coefficient, k^*, are calculated using the Sutherland's law together with a constant Prandtl number, Pr.

$$\mu^*(T^*) = \mu_r^*(\frac{T^*}{T_r^*})^{3/2}\frac{T_r^* + T_s^*}{T^* + T_s^*} \qquad (7)$$

$$k^*(T^*) = \frac{\mu^*(T^*)c_p^*}{Pr} \qquad (8)$$

where $\mu_r^* = 1.7894 \times 10^{-5}$ N $-$ s/m^2, $T_r^* = 288.0$ K, $T_s^* = 110.33$ K. c_p^* is the specific heat at constant pressure. In this paper, the dimensional flow variables are

non-dimensionalized by the corresponding free-stream parameters, i.e., density ρ^*, temperature T^*, velocities u_1^* and u_2^*, and pressure p^* are non-dimensionalized by ρ_∞^*, T_∞^*, u_∞^*, and $\rho_\infty^* u_\infty^{*2}$, respectively.

The high-order shock-fitting method of Zhong[21, 22] is used to solve the two-dimensional Navier-Stokes equations in a domain bounded by the bow shock and the flat plate. The bow shock is treated as a boundary of the computational domain, which makes it possible for the governing equations to be spatially discretized by high-order finite difference methods. A fifth-order upwind scheme is used to discretize the inviscid flux derivatives. Meanwhile, a sixth-order central scheme is used to discretize the viscous flux derivatives. The Rankine-Hugoniot relation across the shock and a characteristic compatibility relation from behind the shock are combined to solve the flow variables behind the shock. By using the shock-fitting method, the interaction between the bow shock and forcing disturbances is solved as a part of solutions with the position and velocity of the shock front being taken as independent flow variables. A three-stage semi-implicit Runge Kutta method of Zhong et al.[23, 24] is used for temporal integration. In the leading edge region, there exists a singular point at the tip of the plate, which introduces numerical instability when the fifth-order shock-fitting method is used to simulate the flow. Therefore, the computational domain for the shock-fitting simulation starts from a very short distance downstream of the leading edge. A second-order TVD code of Zhong and Lee[25] is used to simulate the steady base flow in a small region including the leading edge to supply inlet conditions for the shock-fitting simulation. For unsteady simulation, forcing disturbances are introduced in a downstream region where the shock-fitting method is used.

Flow conditions and forcing model

The free-stream flow conditions for currently studied flow are the same as those used by Maslov et al.[1] in their experiments, i.e.,

$$\begin{array}{ll} M_\infty = 5.92\,, & T_\infty^* = 48.69K\,, \\ p_\infty^* = 742.76Pa\,, & Pr = 0.72\,, \\ f^* = 50kHz\,, & \mathrm{F} = 3.0\times10^{-5}\,, \\ Re_\infty^* = \rho_\infty^* u_\infty^*/\mu_\infty^* = 13\times10^6/m & \end{array}$$

The dimensional coordinate x^* can be easily converted to the dimensionless local Reynolds number by

$$Re_x = Re_\infty^*\, x^* \tag{9}$$

where Re_∞^* is the unit Reynolds number defined as

$$Re_\infty^* = \rho_\infty^* u_\infty^*/\mu_\infty^* \tag{10}$$

In linear stability studies of boundary-layer flows, the Reynolds number based on the local length scale of boundary-layer thickness, L^*, is generally used. They are expressed as

$$R = \frac{\rho_\infty^* u_\infty^* L^*}{\mu_\infty^*} \tag{11}$$

$$L^* = \sqrt{\frac{\mu_\infty^* x^*}{\rho_\infty^* u_\infty^*}} \tag{12}$$

Hence, the relation between R and local Reynolds number Re_x is given by

$$R = \sqrt{Re_x} \tag{13}$$

For the simulation of steady base flow, the wall is adiabatic, and the physical boundary condition of velocity on the flat plate is the non-slip condition. When forcing disturbances of wall oscillation and wall blowing-suction are enforced on the steady base flow, the isothermal temperature condition, which is a standard boundary condition for theoretical and numerical studies of high frequency disturbances, is applied on the wall. Meanwhile, non-slip condition is applied on the wall except the forcing region where stream-wise or wall-normal velocity disturbances are introduced. On the other hand, when forcing disturbances of energy perturbation are enforced, the isothermal temperature condition is applied on the wall except the forcing region where temperature disturbances are introduced. Meanwhile, non-slip condition is applied on the wall. Inlet conditions are specified, while high-order extrapolation is used for outlet conditions because the flow is hypersonic at the exit boundary except a small region near the flat plate.

In Maslov et al.'s[1] experiments, leading-edge receptivity of the Mach 5.92 flow on a flat plate to both two-dimensional and three-dimensional disturbances is investigated. For numerical simulation in this paper, we study the two-dimensional case, which is schematically shown in Fig. 2. The horizontal and vertical distances between the leading edges of the source plate and the test plate are 99 mm and 18.8 mm, respectively. An electric pulse generator with the center located at $x^* = 35$ mm is used to introduce disturbances to the steady base flow. It generates high-voltage electric pulses with duration of 2μs and a frequency of 50 kHz. Experimental results show that the disturbances are introduced by a local glow discharge through an aperture on the source plate when the voltages on the electrodes are low (600 V). On the other hand, when the voltages on the electrodes are increased to 700 V, the size of the glow discharge increases and a flat streamwise extended oval is also observed. Maslov et al. analyzed the properties of the forcing disturbances and concluded that the glow discharge introduces disturbances through a blowing-suction mechanism, while the flat oval on the plate introduces thermal energy.

According to the properties of the electric pulse generator used in Maslov et al.'s experiments, a disturbance model is proposed in this paper, which consists

of stream-wise velocity, wall-normal mass flux, and temperature perturbations. The model is mathematically expressed as

$$\begin{pmatrix} u^{*\prime} \\ (\rho v)^{*\prime} \\ T^{*\prime} \end{pmatrix} = \begin{pmatrix} Q_u \epsilon_1 F(l_1) u_w^{*\prime} \\ Q_v \epsilon_2 G(l_2) (\rho u)_\infty^* \\ Q_T \epsilon_3 H(l_3) T_\infty^* \end{pmatrix} S(t^*) \qquad (14)$$

where $u_w^{*\prime} = (du^*/dy^*)_{y^*=0}$ is the derivative of stream-wise velocity on the plate of the unperturbed steady base flow. $(\rho u)_\infty^*$ and T_∞^* are the mass flux and temperature in free-stream, respectively. Q_u, Q_v, and Q_T are three constants with the value of either 1 or 0. The group of (Q_u, Q_v, Q_T) represents a case with specific forcing disturbances. For example, $(1, 0, 0)$ is the case of wall oscillation, $(0, 1, 0)$ is the case of blowing-suction on the plate, whereas $(0, 0, 1)$ is the case of energy perturbation on the wall. ϵ_1, ϵ_2, and ϵ_3 are small parameters representing the dimensionless amplitudes of perturbations. $F(l_1), G(l_2)$, and $H(l_3)$ are the profile functions of perturbations, where the variables l_1, l_2, and l_3 are dimensionless coordinates defined within the forcing region ($x_i^* \le x^* \le x_e^*$). x_i^* and x_e^* are the coordinates of the leading and trailing edges of the forcing region. In Maslov et al's experiments, x_i^* and x_e^* are equal to 33 mm and 37 mm, respectively. $S(t^*)$ is a time-periodic step function defined as

$$S(t^*) = \begin{cases} 1.0 & \text{if } mod(t^*, 20\mu\text{s}) \le 2\mu\text{s} \\ 0.0 & \text{if } mod(t^*, 20\mu\text{s}) \ge 2\mu\text{s} \end{cases} \qquad (15)$$

where *mod* is a residual function. The value 20μs is the period of the forcing disturbance at a frequency of 50 kHz. Figure 3 plots the time-periodic step function $S(t^*)$ versus time t^* for five periods. It shows that the forcing disturbances are introduced to the steady base flow only within a short time (2μs) in a period (20μs), because the electric pulse used in the experiments has a duration of 2μs.

The profile function of the stream-wise velocity perturbation, $F(l_1)$, can be expressed as

$$\begin{aligned} F(l_1) &= -20.25 l_1^5 + 35.4375 l_1^4 - 15.1875 l_1^2 \\ F(l_1) &= F(l_1)/2.45688 \end{aligned} \qquad (16)$$

where the variable l_1 is defined as

$$l_1 = \begin{cases} 2 \times 0.620287 \times (x^* - x_i^*)/(x_e^* - x_i^*) \\ \text{if } x^* \le 35\text{mm} \\ 2 \times 0.620287 \times (x_e^* - x^*)/(x_e^* - x_i^*) \\ \text{if } x^* \ge 35\text{mm} \end{cases} \qquad (17)$$

In Eq. (16), the constant (2.45688) is the value of $F(l_1)$ at $l_1 = 0.620287$, which is used to normalize the profile function. Figure 4 shows the profile function $F(l_1)$ and the variable l_1 within the forcing region. It is clearly shown that both $F(l_1)$ and l_1 are symmetric within the region 33 mm $\le x^* \le$ 37 mm. The negative values of $F(l_1)$ indicate that the stream-wise velocity perturbation is towards the leading edge of the flat plate. It also shows that the specific 5th-order-polynomial profile function makes the perturbation at the edges (x_i^* and x_e^*) smooth.

The profile function of the blowing-suction perturbation, $G(l_2)$, is the same as what we have used in the receptivity study of a Mach 8 flow over a sharp wedge to wall blowing-suction[17, 18], i.e.,

$$\begin{aligned} G(l_2) &= \begin{cases} 20.25 l_2^5 - 35.4375 l_2^4 + 15.1875 l_2^2 \\ \text{if } l_2 \le 1 \\ -20.25(2 - l_2)^5 + 35.4375(2 - l_2)^4 \\ -15.1875(2 - l_2)^2 \quad \text{if } l_2 \ge 1 \end{cases} \\ G(l_2) &= G(l_2)/2.45688 \end{aligned} \qquad (18)$$

with the variable l_2 being expressed as

$$l_2 = \frac{2(x^* - x_i^*)}{x_e^* - x_i^*} \qquad (19)$$

Again, the constant (2.45688) in Eq. (18) is the value of the profile function at $l_2 = 0.620287$, which is used to normalize $G(l_2)$. Figure 5 shows the profile function $G(l_2)$ and the variable l_2 within the forcing region. It is shown that $G(l_2)$ is anti-symmetric within the region 33 mm $\le x^* \le$ 37 mm, while l_1 is linear. The specific 5th-order-polynomial profile function makes the perturbation at the edges (x_i^* and x_e^*) smooth. Due to the anti-symmetric property of the profile function, the net mass flux introduced to the boundary layer is zero at any instant.

In the current study, four different profile functions of temperature perturbation on the wall are tested to achieve a more reasonable model. They are defined as $H_1(l_3), H_2(l_3), H_3(l_3)$, and $H_4(l_3)$, respectively. For $H_1(l_3)$, the profile of temperature perturbation is the opposite of the stream-wise velocity perturbation given by Eq. (16), i.e., the temperature perturbation is positive within the forcing region.

$$\begin{aligned} H_1(l_3) &= 20.25 l_3^5 - 35.4375 l_3^4 + 15.1875 l_3^2 \\ H_1(l_3) &= H_1(l_3)/2.45688 \end{aligned} \qquad (20)$$

The constant (2.45688) is the value of $H_1(l_3)$ at $l_3 = 0.620287$, which is used to normalize the profile function. The variable l_3 is defined exactly the same as l_1 in Eq. (17).

For $H_2(l_3)$, the temperature perturbation is assumed to be uniformly distributed within the forcing region. Therefore, the profile function is expressed as

$$H_2(l_3) = 1.0 \qquad (21)$$

where l_3 can be an arbitrarily defined dimensionless coordinate. As an example, it can be defined as

$$l_3 = \frac{x^* - x_i^*}{x_e^* - x_i^*} \qquad (22)$$

$H_3(l_3)$ is mathematically expressed as

$$H_3(l_3) = (1.0 - \cos(\pi l_3))/2 \qquad (23)$$

In this case, l_3 is defined as

$$l_3 = \begin{cases} 2 \times (x^* - x_i^*)/(x_e^* - x_i^*) & \text{if } x^* \leq 35\text{mm} \\ 2 \times (x_e^* - x^*)/(x_e^* - x_i^*) & \text{if } x^* \geq 35\text{mm} \end{cases} \quad (24)$$

The fourth profile function of temperature perturbation, $H_4(l_3)$, is expressed as

$$H_4(l_3) = \frac{erf(2.6/\sqrt{2}) - erf(l_3/\sqrt{2})}{erf(2.6/\sqrt{2})} \quad (25)$$

where erf is the error function. The dimensionless coordinate l_3 is defined as

$$l_3 = 2.6 - \begin{cases} 2 \times 2.6 \times (x^* - x_i^*)/(x_e^* - x_i^*) \\ \qquad \text{if } x^* \leq 35\text{mm} \\ 2 \times 2.6 \times (x_e^* - x^*)/(x_e^* - x_i^*) \\ \qquad \text{if } x^* \geq 35\text{mm} \end{cases} \quad (26)$$

In Eqs. (25) and (23), the two constants, $erf(2.6/\sqrt{2}))$ and 2, are used to normalize the profile functions. Figure 6 compares the profile functions of the four different temperature perturbations. The figure shows that the profile functions are all normalized with the maximum values of 1. However, the integral energy perturbation introduced to the steady base flow has the maximum for $H_2(l_3)$ and the minimum for $H_4(l_3)$, because it is proportional to the area surrounded by the profile function and the x^* axis.

Steady Base Flow

In Maslov et al.'s[1] experiments, leading-edge receptivity of the Mach 5.92 flow on a flat plate to both two-dimensional and three-dimensional disturbances was investigated. For two-dimensional disturbances, they firstly investigated the steady base flow over the test plate by removing the source plate. Then the leading-edge receptivity of the test plate was studied by introducing disturbances from the electric pulse generator on the source plate.

Similar to the experiment procedure, the steady base flow over the test plate is firstly simulated by the combination of a fifth-order shock-fitting method and a second-order TVD method. In the leading edge region, there exists a singular point at the tip of the plate, which introduces numerical instability when the fifth-order shock-fitting method is used to simulate the flow. Therefore, the computational domain for the fifth-order shock-fitting method starts at $x^* = 0.0025$ m and ends at $x^* = 0.879$ m, corresponding to $R = 180.28$ and $R = 3380.38$, respectively. In actual simulations, the computational domain is divided into 19 zones with a total of 3746 grid points in stream-wise direction. The number of grid points in wall-normal direction is 121 before $x^* = 0.309$ m and 176 after that location. 41 points are used in the buffering region between two neighboring zones, which has been proved to be sufficient to make the solution accurate and smooth within the whole domain. An exponential stretching function is used in the wall-normal direction to cluster more points inside the boundary layer. On the other hand, the grid points are uniformly distributed in stream-wise direction. The spatial convergency of the results based on this grid structure has been evaluated by grid refinement studies to ensure the grid independence of the fifth-order shock-fitting simulations.

For the first zone, the inlet conditions are obtained from the results of the second-order TVD shock-capturing method which is used to simulate the steady base flow in a small region including the leading edge. For other zones, inlet conditions are interpolated from the results of the previous zone. The domain for the second-order TVD method starts at $x^* = -0.0005$ m and ends at $x^* = 0.0035$ m. Three sets of grid structures are used to check the grid independence of the numerical results. Figure 7 compares the density contours of numerical simulations based on the three sets of grid structures. It shows that the dashdot contours agree well with the dotted contours, while they have discrepancies with the solid contours. This figure indicates that the grid structure 201×176 is enough to ensure the grid independence. However, the grid structure 161×101 is too coarse to achieve spatial converged numerical results.

Figures 8 and 9 show the density and pressure contours of the steady base flow over the test plate obtained from the second-order TVD method and the fifth-order shock-fitting method, respectively. The flow field including the leading edge is simulated by the TVD method, while the flow field after $x^* = 0.0025$ m is simulated by the shock-fitting method. These figures show that density and pressure contours have a good agreement near the leading edge of the buffering region, which indicates that the TVD solutions are accurate enough to be used as inlet conditions for the fifth-order shock-fitting simulation in the first zone. The small discrepancies of the contours near the bow shock are due to viscous effect. Because of the viscosity, the bow shock has a finite thickness for TVD simulation, while it is infinitely thin for the shock-fitting simulation. In Fig. 9, the discrepancies of pressure contours within the boundary layer are mainly caused by the application of high-order extrapolations to outlet boundary, because the local flow near the plate is subsonic. The combination of the shock-fitting method and the TVD method has also been validated in cases of supersonic and hypersonic steady base flows by Ma & Zhong[26] and Wang & Zhong[18].

Figure 10 shows the pressure contours of the steady base flow over the test plate simulated by the fifth-order shock-fitting method. The upper boundary of the flow field represents the bow shock induced by the displacement thickness of the boundary layer. A part of the pressure field from $x^* = 0.03$ m to $x^* = 0.08$ m is amplified to show clearly the pressure contour within the boundary layer. It is noticed that pressure is al-

most a constant across the boundary layer and along the Mach lines, which is consistent with the theories of the boundary-layer flow and supersonic aerodynamics. At a fixed location (constant x^*), the pressure behind the shock is higher than that on the plate due to the existence of the bow shock.

Figure 11 shows the pressure distributions on the flat plate and behind the bow shock versus x^*. Near the leading edge, there exist great pressure gradients, which is induced by the interaction between the inviscid outer flow and the viscous boundary layer. From upstream to downstream, the inviscid/viscous interaction becomes weaker with the bow shock moves away from the boundary layer. As a result, the pressure approaches a constant value further downstream with the pressure gradient decreasing. Again, Fig. 11 shows that the pressure behind the shock is higher than that on the plate at a fixed location (constant x^*). Figure 12 shows the bow shock position and Mach number distribution behind the shock. The dramatic increase of Mach number near the leading edge is also due to the interaction between the inviscid outer flow and the viscous boundary layer. After $x^* > 33$ mm, the intensity of the inviscid/viscous interaction decreases quickly with the blow shock moving away from the boundary layer. The Mach number behind the shock approaches a constant downstream. The increase of Mach number indicates that the bow shock becomes weaker from upstream to downstream.

In order to evaluate the accuracy of numerical simulation, the steady base flow simulated by the fifth-order shock-fitting method is compared with the experimental results. According to Maslov et al.'s experiments, the effect of the inviscid/viscous interaction is strong within the region 0.2 mm $< x^* <$ 33 mm. Figures 11 and 12 show that wall pressure and Mach number behind the shock have large gradients upstream of the location of $x^* = 50$ mm, which is consistent with the experiments.

Figures 13 and 14 compare the normalized Mach number M/M_∞ and dimensionless stream-wise velocity u^*/u^*_∞ versus Blasius coordinates ($\eta = y^*/(x^*/Re^*_\infty)^{1/2}$) at three different locations ($x^* = 96$ mm, 121 mm, and 138 mm). The solid lines represent the distributions of M/M_∞ and u^*/u^*_∞ obtained by solving the compressible boundary-layer equations. Due to the fact that the solution of boundary-layer equations is self-similar, the distributions of M/M_∞ and u^*/u^*_∞ at different locations are exactly the same for the boundary-layer solution. The symbols represent corresponding experimental results of Maslov et al., while the other three lines are corresponding numerical results simulated by the shock-fitting method. The good agreement between the simulation results indicate that a gradientless flow with a self-similar boundary layer is obtained over the test plate, which is evaluated in Maslov et al.'s paper by comparing the experimental results. The gradientless flow is clearly shown in Figs. 11 and 12. Figures 13 and 14 show that the numerical results agree well with the experimental results and the boundary-layer solution near the plate. However, in the region of $\eta > 5$, the numerical results have a better agreement with the experimental results. The difference between the numerical results and the boundary-layer solution is mainly caused by the existence of the bow shock, because the effect of the shock is neglected in the calculation of the compressible boundary-layer equations. Therefore, the effect of the bow shock needs to be considered for supersonic and hypersonic flows.

Figure 15 shows the distributions of dimensionless stream-wise velocity at the three different locations. It shows that the thickness of the boundary layer increases with the location shifting downstream. At $x^* = 96$ mm, 121 mm, and 138 mm, the thicknesses of the boundary layer are approximately 18.4 mm, 20.4 mm, and 22 mm, which agrees well with Maslov et al.'s experimental results of 18 mm, 20 mm, and 22 mm, respectively. The analysis of Figs. 13, 14, and 15 indicate that the fifth-order shock-fitting method is accurate to simulate the hypersonic flow considered in the current study.

In the stability study of the hypersonic flow, the characteristics of the steady base flow is of great importance. For example, the profiles of stream-wise velocity and temperature, and their corresponding first- and second-order derivatives are important to the boundary-layer normal modes obtained by solving the boundary-layer stability equations. In the current study, the numerical steady base flow at three different locations ($x^* = 96$ mm, 121 mm, and 138 mm) are compared. Figure 16 shows the distributions of the dimensionless temperature versus Blasius coordinates. The first- and second-order derivatives of stream-wise velocity and temperature are shown in Figs. 17 and 18, respectively. These figures show that the derivatives of u^*/u^*_∞ and T^*/T^*_∞ have small oscillations at the edge of the boundary layer, which may be caused by the interaction between the inviscid outer flow and the viscous boundary layer. It is noticed that the temperature distribution and the derivatives of u^*/u^*_∞ and T^*/T^*_∞ at the three different locations have a good agreement. Again, such an agreement indicates that a gradientless flow with a self-similar boundary layer is obtained over the test plate.

Unsteady simulation results

In order to evaluate the forcing disturbance model of Eq. (14) and further evaluate the accuracy of the numerical simulation, forcing disturbances are introduced to the steady base flow through a slot on the plate with the leading and trailing edges at $x^*_l = 33$ mm and $x^*_e = 37$ mm. Specifically, six cases of different forcings are considered. In each case, disturbances at the frequency of 50 kHz is introduced. The values of ϵ_1, ϵ_2 and ϵ_3 in Eq. (14) are assigned to be 1.0×10^{-7}, 1.0×10^{-5}, and 1.0×10^{-3}, respectively. The subsequent responses of the hypersonic boundary layer are simulated by the fifth-order shock-fitting method. Details of the forcing

Table 1: Types and profile functions of the forcing disturbances for the six cases considered in the current study

n	(Q_u,Q_v,Q_T)	Profile
1	$(1,0,0)$	$F(l_1)$ as in Eq. (16)
2	$(0,1,0)$	$G(l_2)$ as in Eq. (18)
3	$(0,0,1)$	$H_1(l_3)$ as in Eq. (20)
4	$(0,0,1)$	$H_2(l_3)$ as in Eq. (21)
5	$(0,0,1)$	$H_3(l_3)$ as in Eq. (23)
6	$(0,0,1)$	$H_4(l_3)$ as in Eq. (25)

Table 2: Dimensional and dimensionless amplitudes of the forcing disturbances for the six cases considered in the current study

n	Amplitude	Dimensionless amplitude
1	$8.885 \times 10^{-2} m/s$	1.073×10^{-4}
2	4.401×10^{-4} kg/m$^2 s$	1.0×10^{-5}
3	4.869×10^{-2} K	1.0×10^{-3}
4	4.869×10^{-2} K	1.0×10^{-3}
5	4.869×10^{-2} K	1.0×10^{-3}
6	4.869×10^{-2} K	1.0×10^{-3}

disturbances for the six cases are listed in Tables 1 and 2.

Table 1 shows that case 1 is the case of wall oscillation, case 2 is the case of blowing-suction on the plate, whereas cases $3 \sim 6$ are the cases of energy perturbations on the wall. In Table 2, the dimensional amplitudes of the six different forcing disturbances are obtained from Eq. 14. They are non-dimensionalized by the corresponding free-stream variables: $u^*_\infty = 827.974$ m/s, $(\rho u)^*_\infty = 44.01$ kg/m^{2}s, and $T^*_\infty = 48.69$ K, respectively. The amplitudes of the temperature disturbances of cases $3 \sim 6$ are the same, because the profile functions $H_1(l_3), H_2(l_3), H_3(l_3)$, and $H_4(l_3)$ are all normalized with the maximum values of 1, which is shown clearly in Fig. 6.

Figure 19 shows the contours of dimensionless instantaneous pressure perturbations induced by different forcing disturbances of the six cases considered in the current paper. Specifically, Figs. 19(a) and 19(b) show the results of wall oscillation and wall blowing-suction, respectively. Figures 19(c) to 19(f) show the results of energy perturbations with the four different profile functions. It is noticed that the structures of the perturbation fields in Figs. 19(c) to 19(f) are similar, while they are different from those of Figs. 19(a) and 19(b) due to the properties of different forcing disturbances. All the figures show that the excited pressure perturbations are divided into two branches downstream of the forcing slot. One branch propagates along the Mach lines outside the boundary layer (acoustic waves), while the other branch stays within the boundary layer which is dominated by mode S. The wave structure in the boundary layer is typical of mode S wave for the hypersonic flow.

In order to check the amplitudes of the pressure perturbations, fast Fourier transformation (FFT) is applied to the dimensionless instantaneous pressure perturbations. In the Fourier domain, the freqency of 50 kHz and its higher harmonics are considered. Specifically, the frequencies can be expressed as

$$f^*_N = 50N\text{kHz} \tag{27}$$

where $N \in \{1, 15\}$. f^*_1 is the base frequency, while the other fourteen frequencies are higher harmonics.

Figure 20 shows the amplitude distributions along the plate of pressure perturbations at the frequency of 50 kHz and its higher harmonics induced by different forcing disturbances of the six cases. Specifically, Figs. 20(a) and 20(b) show the numerical results of wall oscillation and wall blowing-suction, respectively. Figures 20(c) to 20(f) show the results of energy perturbations with the four different profile functions. The numbers of 1 to 7 in the figures represent the frequencies f^*_1 to f^*_7. It is clearly shown in all six figures that the pressure perturbations of the frequencies (f^*_N, $N \in \{8, 15\}$) are comparably weak. Downstream of the forcing region, the harmonic of the frequency $f^*_5 = 250$ kHz has the maximum perturbation amplitude. The figures also show that the pressure perturbations of wall blowing-suction is higher than that of wall oscillation. In turn, the pressure perturbations of wall oscillation is higher than that of energy perturbations.

Figures 21 and 22 compare the normalized pressure perturbation amplitudes of the cases 1, 2, and 3 at the frequencies of $f^*_1 = 50$ kHz and $f^*_5 = 250$ kHz, respectively. $(p\prime^*/p^*_\infty)_{nl}$ is the normalized pressure perturbation amplitude obtained by dividing the perturbation amplitudes with the corresponding dimensionless amplitudes listed in Table 2. Again, these figures show that the pressure perturbations of wall blowing-suction is higher than that of wall oscillation. In turn, the pressure perturbations of wall oscillation is higher than that of energy perturbations. The boundary layer is much more sensitive to blowing-suction disturbances than to wall oscillation and enery perturbation. These results are consistent with those of Fedorov and Khokhlov[27].

Figures 23 and 24 compare the dimensionless pressure perturbation amplitudes of the cases 3, 4, 5, and 6 at the frequencies of $f^*_1 = 50$ kHz and $f^*_5 = 250$ kHz, respectively. These figures show that the perturbation amplitudes of case 4 are higher than those of the other cases. The perturbation amplitudes of cases 3 and 5 are approximately the same, and they are higher than those of case 6. Recall what have been discussed for Fig. 6, the integral energy perturbation introduced to the steady base flow has the maximum for case 4 and

the minimum for case 6. It can be concluded that the amplitude of the pressure perturbation to energy perturbation is proportional to the energy introduced to the steady base flow.

Summary

The objective of this study is to numerically investigate the steady base flow and the receptivity of the hypersonic boundary layer, and to evaluate the accuracy of the numerical simulation by comparing the results of numerical simulations and experiments. The steady base flow is simulated by solving the two-dimensional Navier-Stokes equations with a combination of a fifth-order shock-fitting method and a second-order TVD method. According to the properties of the electric pulse generator used in Maslov et al.'s experiments, a model of forcing disturbances is proposed. For unsteady simulations, disturbances of six different cases are introduced to the steady base flow by a forcing slot located on the flat plate. The subsequent responses of the hypersonic boundary layer are simulated by the fifth-order shock-fitting method.

The main conclusions of the current study are:

- The numerical solution to the steady base flow is compared with that of the experiment. The good agreement between the two sets of steady base flows indicates that the numerical simulation of the fifth-order shock-fitting method is accurate for the hypersonic flow simulation.
- The hypersonic boundary-layer flow is much more sensitive to blowing-suction disturbances than to wall oscillations and energy perturbations. The pressure perturbations of wall blowing-suction is higher than that of wall oscillation. In turn, the pressure perturbations of wall oscillation is higher than that of energy perturbations.
- The amplitude of the pressure perturbation to energy disturbances is proportional to the energy introduced to the steady base flow.

The unsteady simulations in a large domain and the leading-edge receptivity of the hypersonic boundary layer will be further studied. And more cases of the forcing disturbances will be used to test the disturbance model proposed in the paper.

Acknowledgments

This work was sponsored by the Air Force Office of Scientific Research, USAF, under AFOSR Grant #FA9550-04-1-0029, monitored by Dr. John Schmisseur. The views and conclusions contained herein are those of the authors and should not be interpreted as necessarily representing the official policies or endorsements either expressed or implied, of the Air Force Office of Scientific Research or the U.S. Government.

References

[1] A. A. Maslov, A. N. Shiplyuk, A. Sidorenko, and D. Arnal. Leading-edge receptivity of a hypersonic boundary layer on a flat plate. *Jounral of Fluid Mechanics*, 426, pp.73-94, 2001.

[2] M. R. Malik. Boundary-Layer Transition Prediction Toolkit. *AIAA paper 97-1904*, 1997.

[3] M. E. Goldstein and L. S. Hultgren. Boundary-layer receptivity to long-wave free-stream disturbances. *Annual Review of Fluid Mechanics*, Vol. 21, pp. 137-166, 1989.

[4] L. M. Mack. Linear Stability Theory and the Problem of Supersonic Boundary-Layer Transition. *AIAA Journal*, 13, No. 3, pp. 278-289, 1975.

[5] A. V. Fedorov and A. P. Khokhlov. Excitation of unstable modes in a supersonic boundary layer by acoustic waves. *Fluid Dynamics (Historical Archive)*, 26, pp.531-537, 1991.

[6] A. V. Fedorov and A. P. Khokhlov. Sensitivity of a supersonic boundary layer to acoustic disturbances. *Fluid Dynamics (Historical Archive)*, 27, pp.29-34, 1992.

[7] A. Demetriades. An experiment on stability of hypersonic laminar boundary layers. *Journal of Fluid Mechanics*, 7, pp.385-396, 1960.

[8] J. Laufer and T. Vrebalovich. Stability and transition of a supersonic laminar boundary layer on an insulated flat plate. *Journal of Fluid Mechanics*, 9, pp.257-299, 1960.

[9] J. M. Kendall. Wind Tunnel Experiments Relating to Supersonic and Hypersonic Boundary-Layer Transition. *AIAA Journal*, 13, No. 3, pp. 290–299, 1975.

[10] A. D. Kosinov and A. A. Maslov. Growth of artificially induced disturbances in a supersonic boundary layer. *Fluid Dynamics (Historical Archive)*, 19, No.5 pp.703-709, 1984.

[11] A. A. Maslov and N. V. Seminov. Excitation of natural oscillations in a boundary layer by an external acoustic field. *Fluid Dynamics (Historical Archive)*, 21, pp.400-404, 1986.

[12] X. Zhong. Receptivity of hypersonic boundary layers to freestream disturbances. *AIAA paper 2000-0531*, January 2000.

[13] Y. Ma and X. Zhong. Receptivity of a supersonic boundary layer over a flat plate. Part 1:Wave Structures and Interactions. *Journal of Fluid Mechanics*, 488, pp.31-78, 2003.

[14] Y. Ma and X. Zhong. Receptivity of a supersonic boundary layer over a flat plate. Part 2:Receptivity to Freestream Sound. *Journal of Fluid Mechanics*, 488, pp.79-121, 2003.

[15] Y. Ma and X. Zhong. Receptivity of a supersonic boundary layer over a flat plate. Part 3. Effects of different types of free-stream disturbances. *Journal of Fluid Mechanics*, 532, pp.63-109, 2005.

[16] I. V. Egorov, A. V. Fedorov, and V. G. Soudakov. Direct Numerical Simulation of Unstable Disturbances in Supersonic Boundary Layer. *AIAA paper 2004-0588*, January 2004.

[17] X. Wang and X. Zhong. Receptivity of a supersonic boundary layer over a sharp wedge to wall blowing/suction. *AIAA paper 2004-0254*, January 2004.

[18] X. Wang and X. Zhong. Receptivity of A Mach 8.0 Flow over A Sharp Wedge to Wall Blowing-Suction. *AIAA paper 2005-5025*, June 2005.

[19] A. Tumin, X. Wang, and X. Zhong. DNS and the theory of receptivity in a hypersonic boundary layer. *APS 58th Annual Meeting of the Division of Fluid Dynamics*, November 2005.

[20] A. Tumin, X. Wang, and X. Zhong. Direct Numerical Simulation of Receptivity in a Hypersonic Boundary Layer: Validation. *AIAA paper 2006-1108*, January 2006.

[21] X. Zhong. Direct Numerical Simulation of Hypersonic Boundary-Layer Transition Over Blunt Leading Edges, Part I: New Numerical Methods and Validation (Invited). *AIAA paper 1997-0755, 35th AIAA Aerospace Sciences Meeting and Exhibit, January 6-9, Reno, Nevada*, 1997.

[22] X. Zhong. High-Order Finite-Difference Schemes for Numerical Simulation of Hypersonic Boundary-Layer Transition. *Journal of Computational Physics*, 144, pp. 662-709, 1998.

[23] X. Zhong. Additive Semi-Implicit Runge-Kutta Schemes for Computing High-Speed Nonequilibrium Reactive Flows. *Journal of Computational Physics*, 128, pp.19-31, 1996.

[24] K. J. Yoh and X. Zhong. Low-storage semi-implicit runge-kutta methods for reactive flow computations. *AIAA paper 1998-0130*, January 1998.

[25] X. Zhong and T. Lee. Nonequilibrium real-gas effects on disturbance/bow shock interaction in hypersonic flow past a cylinder. *AIAA paper 1996-1856*, January 1996.

[26] Y. Ma and X. Zhong. Receptivity to Freestream Disturbances of Mach 4.5 Flow over A Flat Plate. *AIAA Paper 2002-0140*, January 2002.

[27] A. V. Fedorov and A. P. Khokhlov. Receptivity of Hypersonic Boundary Layer to Wall Disturbances. *Theoretical and Computational Fluid Dynamics*, 15, pp.231-254, 2002.

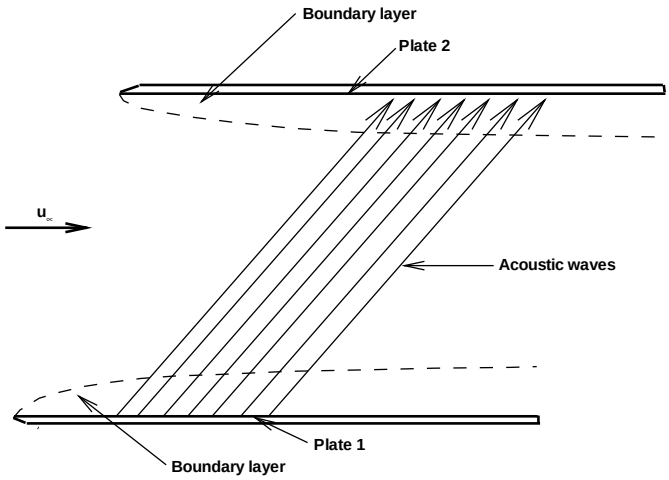

Figure 1: A schematic of the receptivity experiment setup by Maslov and Seminov[11].

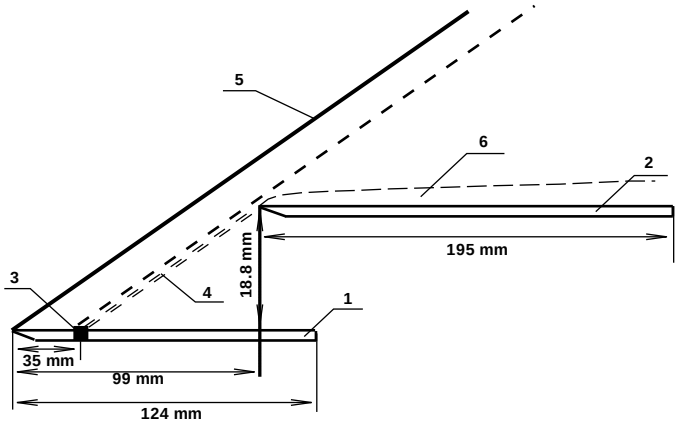

Figure 2: Numerical simulation setup for receptivity of the Mach 5.92 flow to the two-dimensional disturbances (1 - source plate with two-dimensional perturber, 2 - test plate, 3 - disturbances actuator, 4 - acoustic radiation, 5 - bow shock, 6 - boundary layer).

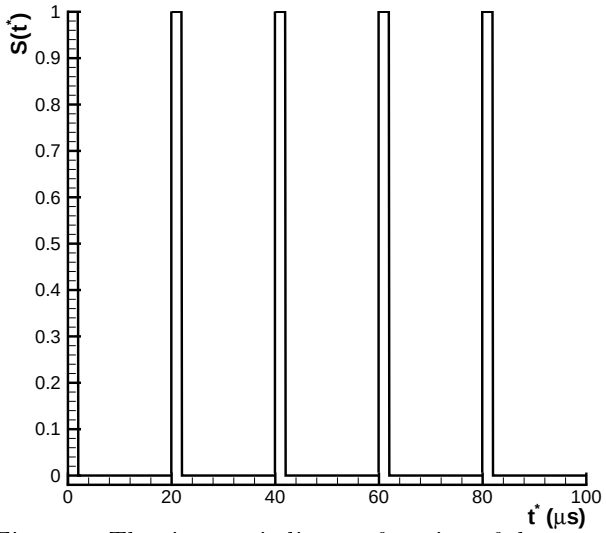

Figure 3: The time-periodic step function of the perturbation model in the current study ($S(t^*)$ vs time (t^*).

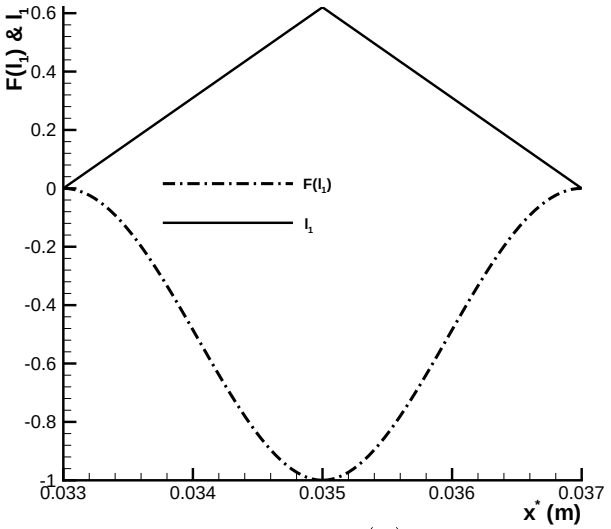

Figure 4: The profile function $F(l_1)$ and the variable l_1 within the perturbation region for the case of a hump.

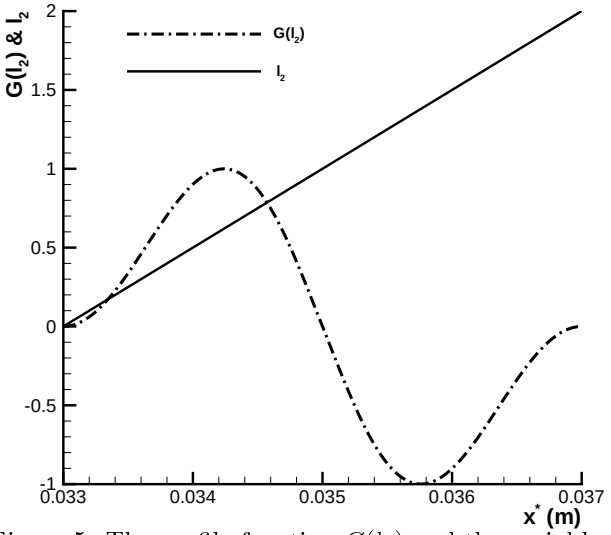

Figure 5: The profile function $G(l_2)$ and the variable l_2 within the perturbation region for the case of blowing-suction.

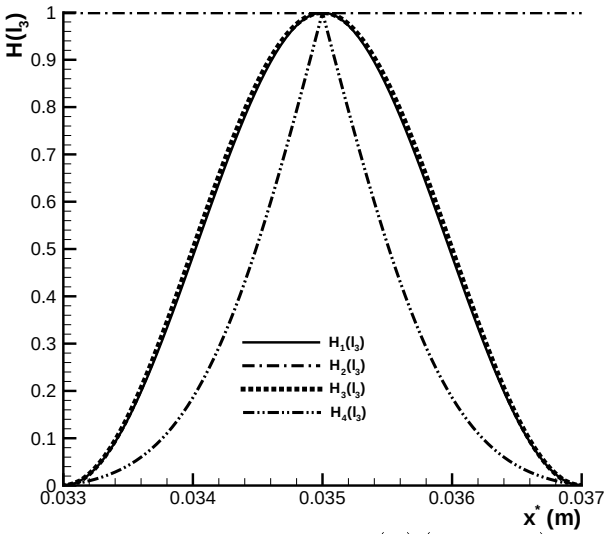

Figure 6: The profile functions $H_i(l_3)$ $(i = 1 \sim 4)$ within the perturbation region for the case of temperature perturbation.

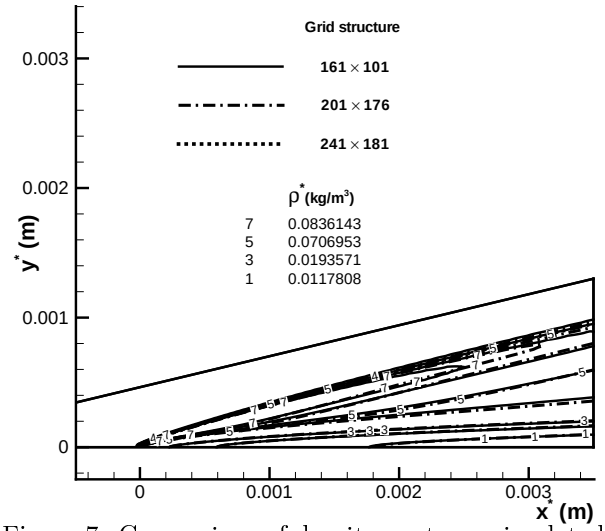

Figure 7: Comparison of density contours simulated by TVD method based on the three sets of grid structures.

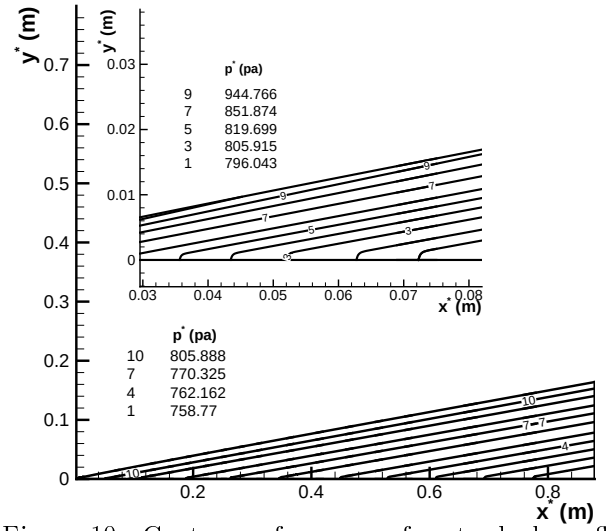

Figure 10: Contours of pressure for steady base flow over the test plate ($M_\infty = 5.92$).

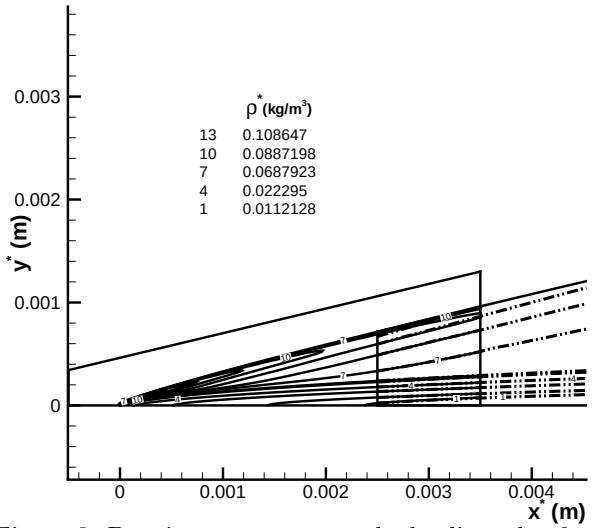

Figure 8: Density contours near the leading edge for the steady base flows over the test plate obtained by TVD method and shock-fitting method.

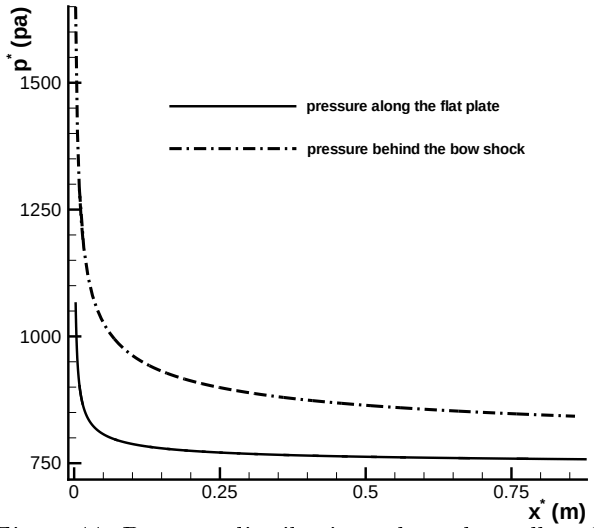

Figure 11: Pressure distributions along the wall surface and behind the shock for steady base flow over the test plate.

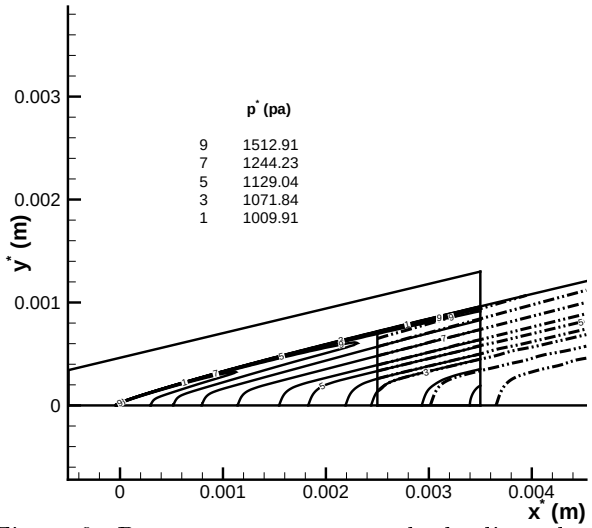

Figure 9: Pressure contours near the leading edge for the steady base flows over the test plate obtained by TVD method and shock-fitting method.

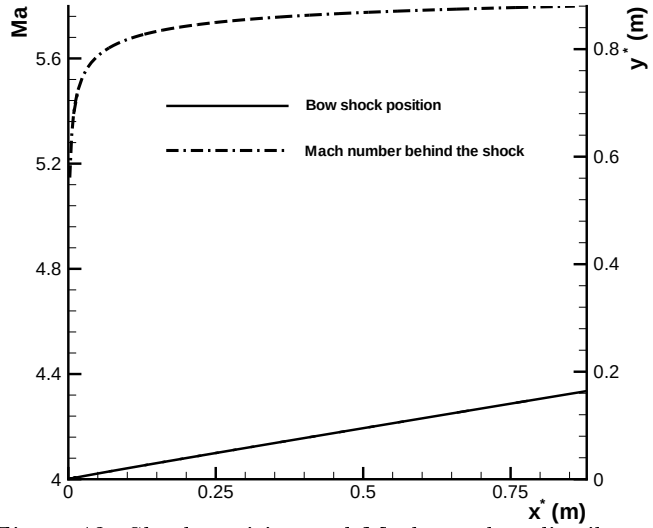

Figure 12: Shock position and Mach number distribution behind the shock for steady base flow over the test plate.

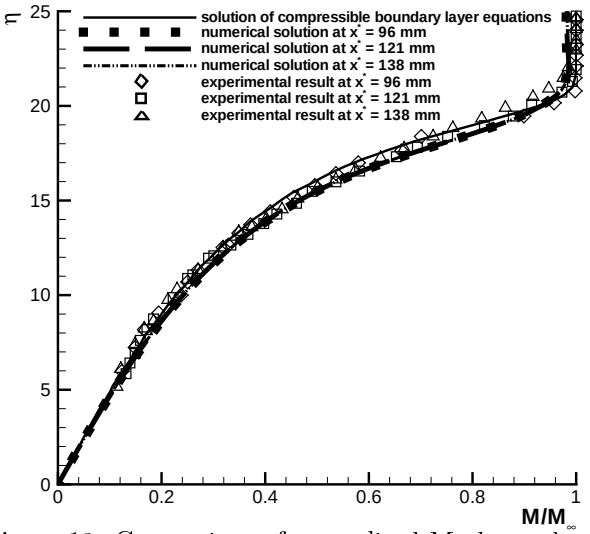

Figure 13: Comparison of normalized Mach number vs Blasius coordinates at three different locations.

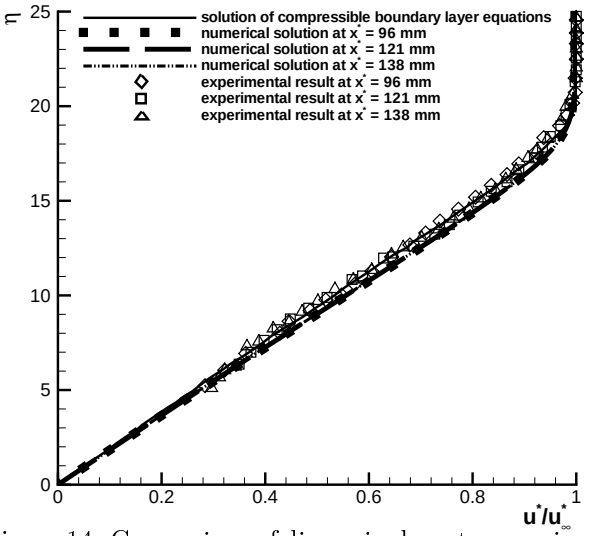

Figure 14: Comparison of dimensionless stream-wise velocity vs Blasius coordinates at three different locations.

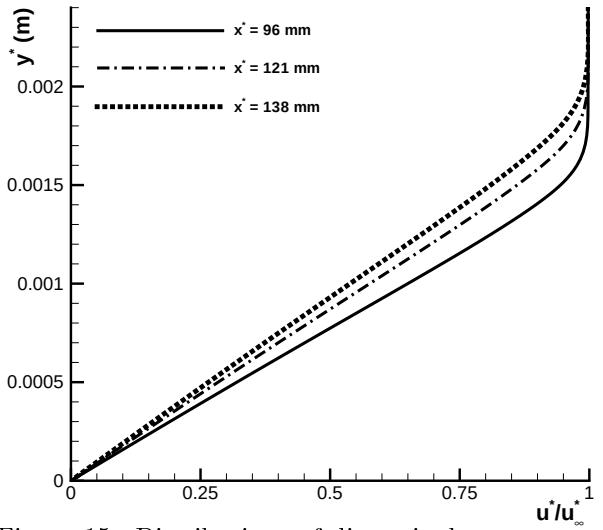

Figure 15: Distributions of dimensionless stream-wise velocity of the steady base flow at three different locations.

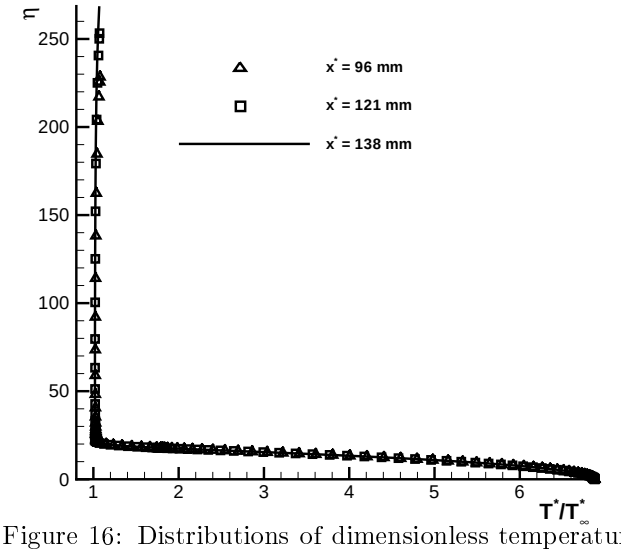

Figure 16: Distributions of dimensionless temperature of the steady base flow at three different locations.

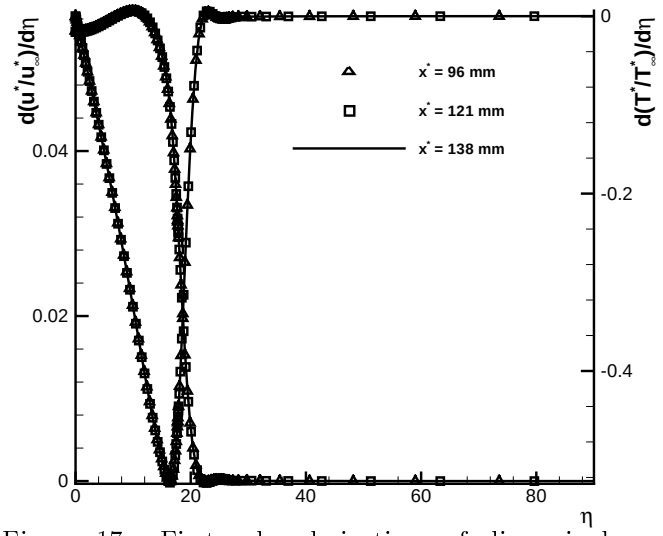

Figure 17: First-order derivatives of dimensionless stream-wise velocity and temperature of the steady base flow.

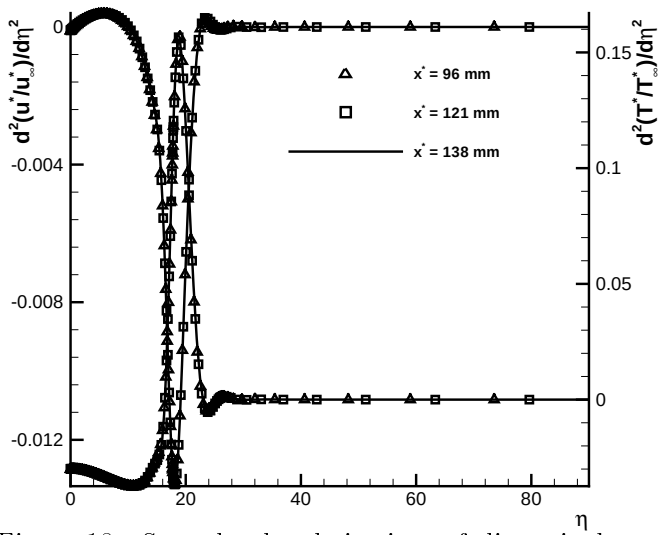

Figure 18: Second-order derivatives of dimensionless stream-wise velocity and temperature of the steady base flow.

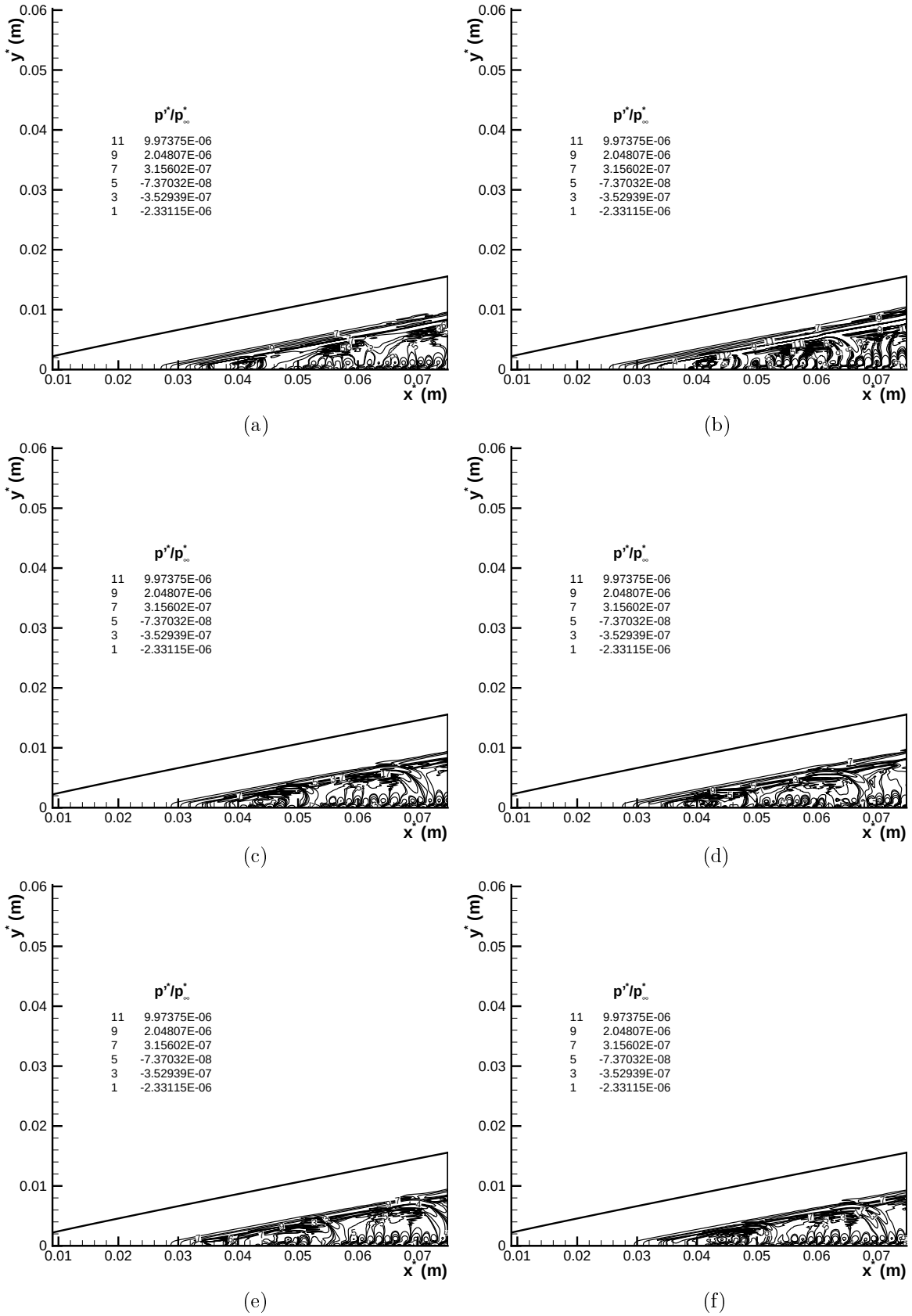

Figure 19: Contours of dimensionless instantaneous pressure perturbations induced by different forcing disturbances of the six cases considered: (a) case 1; (b) case 2; (c) case 3; (d) case 4; (e) case 5; (f) case 6.

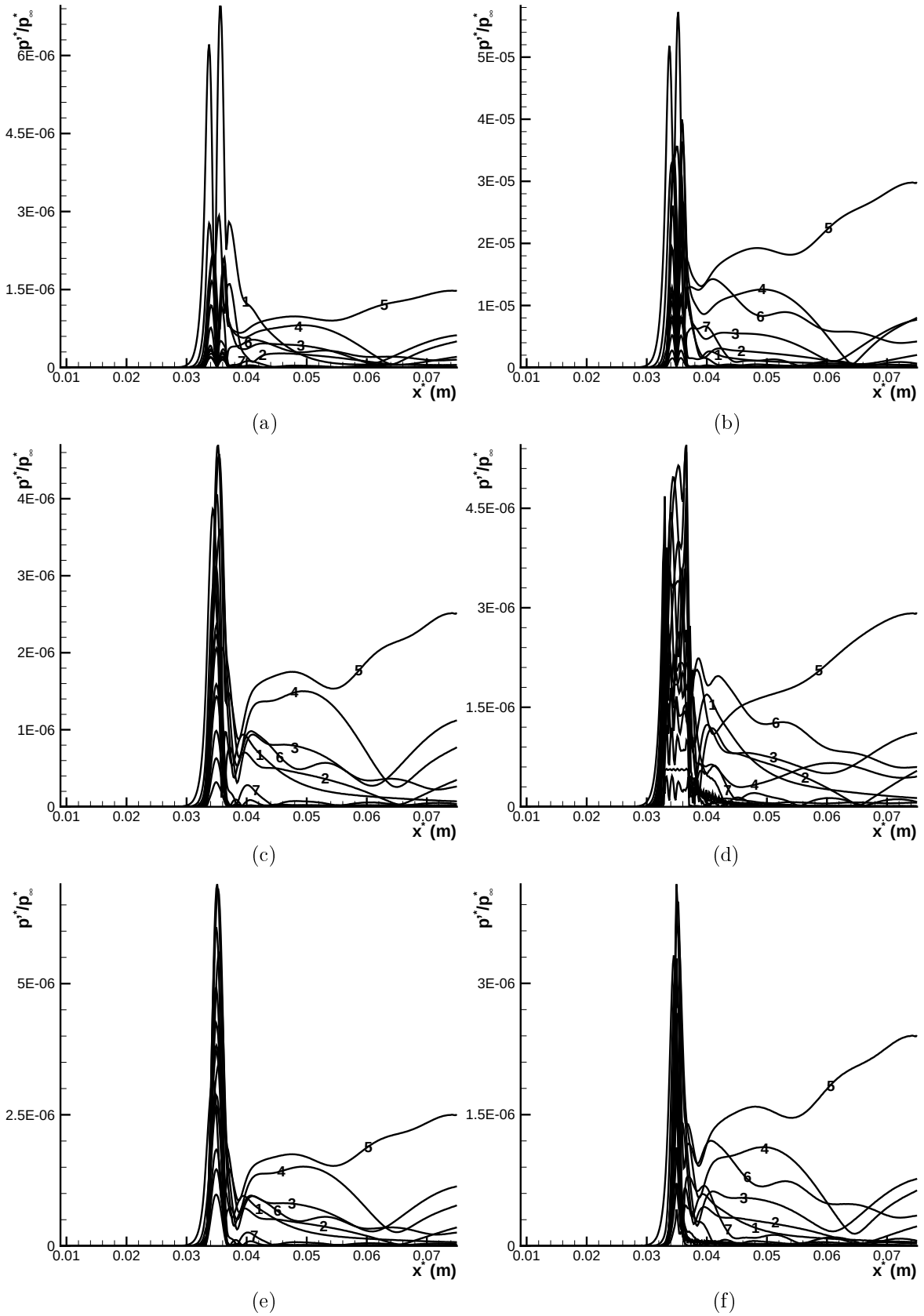

Figure 20: Amplitude distributions along the plate of pressure perturbations at the frequency 50 kHz and its harmonics induced by different forcing disturbances of the six cases considered: (a) case 1; (b) case 2; (c) case 3; (d) case 4; (e) case 5; (f) case 6.

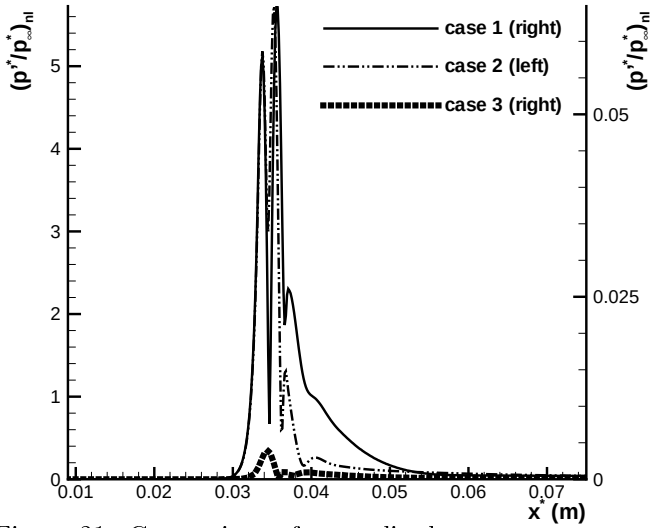

Figure 21: Comparison of normalized pressure perturbation amplitudes of the cases 1, 2, and 3 ($f_1^* = 50$ kHz).

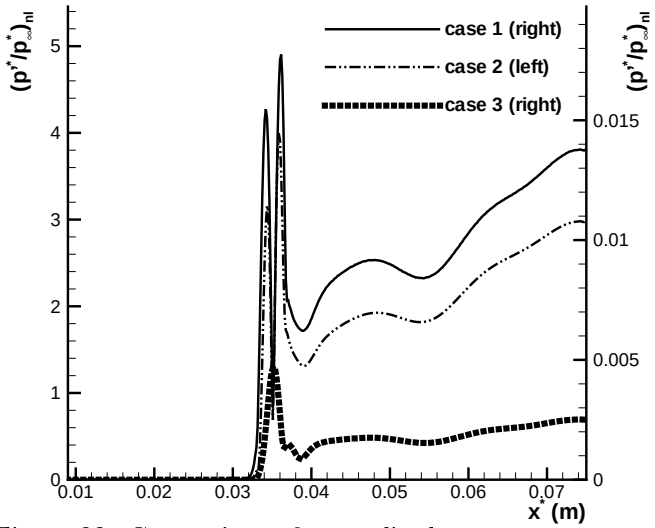

Figure 22: Comparison of normalized pressure perturbation amplitudes of the cases 1, 2, and 3 ($f_5^* = 250$ kHz).

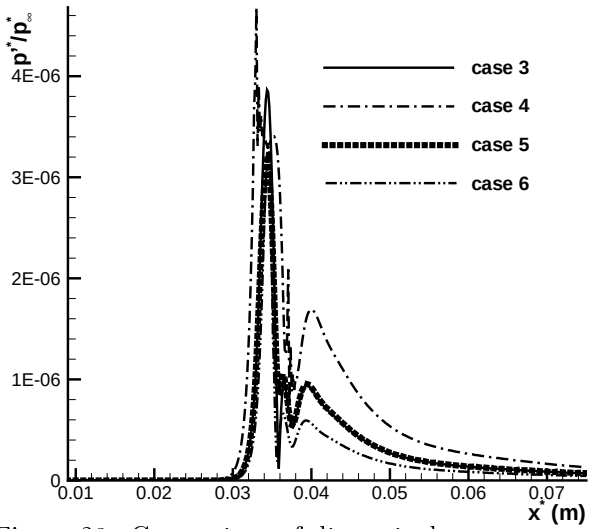

Figure 23: Comparison of dimensionless pressure perturbation amplitudes of the cases 3, 4, 5, and 6 ($f_1^* = 50$ kHz).

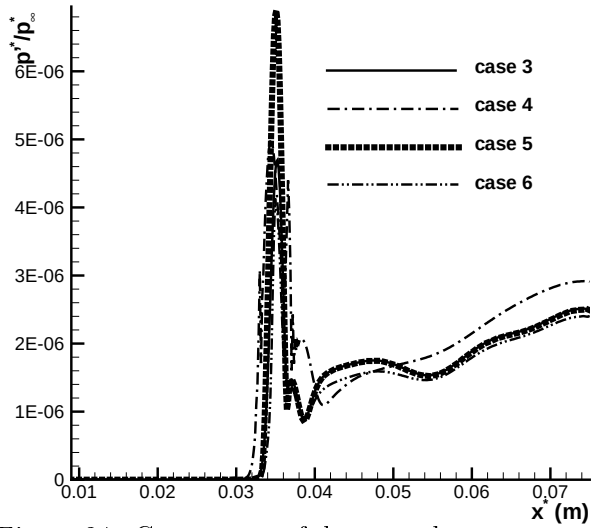

Figure 24: Comparison of dimensionless pressure perturbation amplitudes of the cases 3, 4, 5, and 6 ($f_5^* = 250$ kHz).